Wind and turbulence measurements over sea by Doppler lidar and SAR

Ch. Werner,[1] J. Streicher,[1] O. Reitebuch,[1] E. Nagel,[1] T. Schneiderhan,[2] T. König,[2] S. Lehner,[2] V.A. Banakh,[3] A.V. Falits,[3] A. Dabas,[4] and P. Delville[5]

[1] DLR-Institute of Atmospheric Physics, Oberpfaffenhofen, Germany
[2] DLR-Methodik der Fernerkundung, Oberpfaffenhofen, Germany
[3] Institute of Atmospheric Optics, Siberian Branch of the Russian Academy of Sciences, Tomsk, Russia
[4] Meteo France, Toulouse, France
[5] INSU, Paris, France

The results described in this paper concern the evaluation of wind vector and the atmospheric wind turbulent parameters based on the Doppler lidar and Synthetic Aperture Radar (SAR) data. A spaceborne SAR measures the single level wind vector over sea in a large swath, an airborne Doppler lidar measures a 3D wind profile along the flight track. Comparison of the lidar and SAR estimates of the mean wind and turbulence parameters obtained from the simultaneous lidar and SAR measurements over approximately the same area of the Mediterranean Sea is carried out.

Introduction

Remote sensed wind measurements for a single level, the sea surface, were performing during many years by the European Research Satellite (ERS) scatterometer (SCAT).[1] A remote sensed wind profile, i.e., the horizontal (2D) or 3D wind vector in height intervals from ground to the stratosphere is a new quality since airborne laser Doppler systems are available.[2] This paper describes the combination of single level wind data from satellite-borne Synthetic Aperture Radar (SAR) sensors[3,4] in a large area with a wind profile measured with an airborne Doppler lidar WIND[5,6] along a flight path over that area.

Remote sensing technique can be applied to study the atmospheric wind turbulence as well. It offers certain advantages over conventional *in situ* methods providing adequate spatiotemporal resolution of measurements on large areas. The measurements of turbulent wind field statistics by solid-state coherent Doppler lidars are discussed, in particular, in Refs. 7, 8. Statistics of wind velocity measured by cw CO_2 Doppler lidar and methods of retrieval of the atmospheric turbulence parameters from cw CO_2 Doppler lidar data are studied in Ref. 9. The results of measurement of turbulent wind spectra by ground-based coherent CO_2 pulsed Doppler lidar are presented in Ref. 10.

It this paper we show the results of estimate of the wind turbulent parameters based on calculation of the spatial structure function of fluctuations of line of sight (LOS) component of wind vector, measured by airborne coherent CO_2 Doppler laser system WIND. The results of lidar estimate of the turbulent energy dissipation rate are compared with estimation of the dissipation rate obtained based on the SAR wind velocity data. In the last case the estimation of the dissipation rate is performed by means of parameterization of the spatial spectra of wind velocity determined from SAR data. The parameterization is done on the base of fitting the experimental spectra to the modeled spectra, simulated for the Karman's model of turbulence with spatial resolution, spatial average, and wind shear which took place in the experiment.

1. Doppler lidar

A heterodyne lidar consists of a frequency-stable f_0 laser transmitter locked to the local oscillator via a locking loop, a transmitter and receiver telescope, a heterodyne detector, where the local oscillator radiation is mixed with the Doppler-shifted backscatter signal, and a signal processing system. The signal originates from the backscattering by small aerosol particles which move through the laser sounding volume with the prevailing windspeed. The wind-shifted Doppler frequency Δf_D directly determines the LOS component (V_{LOS}) of the wind vector

$$\Delta f_D = 2\,\frac{V_{LOS}}{c}\,f_0. \tag{1}$$

By scanning the transceiver with a conical scan pattern (VAD) or by using the non scanning operations (LOS) (see Fig. 1) one reaches different azimuth and elevation angles to combine the single LOS components to a wind vector.

At an azimuth angle θ and an elevation angle φ, V_{LOS} is related to the wind vector components u (east-west wind component), v (north-south wind component), and w (vertical wind component) by

$$V_{LOS} = u\sin\theta\cos\varphi + v\cos\theta\cos\varphi + w\sin\varphi. \tag{2}$$
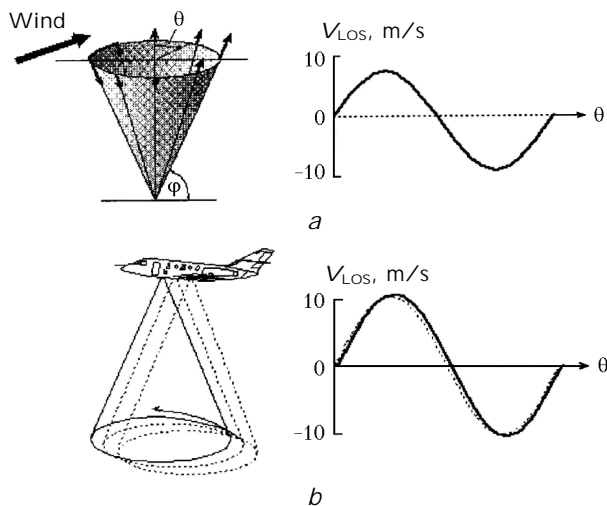
Fig. 1. Principle of ground-based and airborne conical scans.

Caused by the aircraft speed, the Doppler shift Δf_D contains mainly the contribution of the aircraft. For a ground-based system one can determine the wind vector by sine-wave-fitting of Eq. (2).[11] For the airborne system the aircraft component has to be removed before

$$V_{LOS} = V_{LOS} \text{ (wind component)} +$$

$$+ V_{LOS} \text{ (aircraft component)}. \qquad (3)$$

Figure 1 shows the situation for both systems, the ground-based one and the airborne one for a wind speed of about 10 m/s. In Fig. 1 it assumed that the wind has the same direction as the aircraft. For the ground-based system (Fig. 1a) the sine wave fitting gives 3 wind components u, v and w directly (Eq. (2)). For the airborne system (Fig. 1b) the wind component is a minor contribution, the dashed curve is the sum of aircraft velocity contribution and wind (Eq. (3)), the solid curve is the aircraft contribution only. An exact aircraft data system is required to remove this influence.

Airborne Doppler lidars were used in the past[12-16] and are applied also as precursor experiments for spaceborne application of the lidar technique.[17-19]

Coherent Doppler lidar system WIND was developed in a frame of a French—German cooperation. The partners include the Deutsches Zentrum für Luft- und Raumfahrt (DLR), the Centre National de la Recherche Scientifique (CNRS), and the Centre National d'Études Spatiales (CNES).[5,6,10,20] WIND flies on board DLR Falcon 20 jet. Adaptation to CNRS Falcon 20 is under way. Adaptation to the future turbo-prop of Météo-France is envisaged.

The major components of a coherent Doppler lidar WIND are a pulsed transmitter laser (TE laser), optics including a telescope, heterodyne detectors, where the local oscillator beam is mixed with the outgoing pulse for frequency reference, and the Doppler-shifted backscattered signal for radial velocity measurements, a signal processing unit. A locking-loop controls the frequency of the TE laser and maintains a constant

difference of 40 MHz between the local oscillator and the TE laser. The laser pulse of a few microseconds duration and a carrier frequency f_0 is sent out via the transceiver telescope into the atmosphere. The main advantages of the WIND instrument are:

a mechanical frame—enabling lidar operations in a vibrating environment;

an early digitizing concept (to save all data before any processing);

a good synchronization with aircraft position data.

WIND measures the wind (horizontal + vertical component) below the aircraft, from the surface up to the flight altitude. The maximum flight altitude is 11 km. The vertical resolution is 250 m. The horizontal resolution varies as a function of the flight altitude and the signal strength. It is in the range 4 km to 10 km. The basic parameter measured by the Doppler lidar is the LOS wind component. To get wind vectors, the line-of-sight is conically scanned. The sounding laser beam is transmitted through a bottom window of the aircraft at a constant Nadir angle of 30 degrees. It is rotated at the rate of 3 rounds per minute.

The derivation of wind vectors from the LOS wind components assumes the atmosphere is horizontally homogeneous over at least one scan rotation. The two or three wind components are estimated as a function of the altitude by a least-square fit. The accuracy for the wind vectors varies as a function of the aerosol content of the atmosphere. It can be of the order of $50 \text{ cm} \cdot \text{s}^{-1}$ in good conditions, but may degrade to several meters per second in atmospheric volumes poorly loaded with aerosols. The error sources are low aerosol concentration and the chirp of the laser pulse. Chirp means variation in the outgoing pulse frequency characteristics f_0.

2. Radar wind sensor

The determination of the wind over ocean by ERS SCAT is based on radar signal backscattered by water surface. The backscatter from a rough ocean surface for moderate incident angles of 20—60° is explained by the resonant Bragg scattering.[21] The backscatter signal is caused by the water-wave component which is in resonance with the incident radiation. The resonant water wavenumber k_w is related to the electromagnetic wave number k_{el} of the radar according to

$$k_w = 2 \, k_{el} \, \sin\alpha,$$

where α is the incident angle of the radar beam.

For the determination of the wind speed and direction over the ocean surface from the three antennas of the ERS-2 scatterometer an empirical C-band model CMOD4 (Ref. 1) was developed by the European Space Agency. In the case of the ERS-2 SAR, operating in the C-band with incident angles between 20 and 26°, the range of scattering wavelength extends from 8.2 to 6.5 cm. Therefore the normalised radar cross section (NRCS) can be used to evaluate parameters which influence the small-scale roughness, such as the wind speed. The SCAT and SAR on board

ERS-1/2 operate at the same frequency. Thus, the CMOD4 can be applied to the SAR.[3] In contrast to the SCAT, SAR collects data only from one antenna. Therefore, the wind direction is needed as further input to derive the wind speed by CMOD4. Usually, SAR images show distinct features like wind streaks or shadowing behind coasts from which the wind direction can be determined.

One problem when deriving wind speed from ERS SAR images is that the grey levels of the image have to be converted to calibrated normalised radar cross sections. For ERS SAR the calibration was a difficult task due to saturation problems with the analog-to-digital converter that resulted in a power loss. Using recalibration and CMOD4, scatter plots from SAR-derived wind fields and ground-truth data showed a correlation of 0.78.[3]

3. WIND and ERS-2 SAR wind measurement results

Figure 2 shows the available ERS-2 SAR acquisition (swath of the ERS-2 satellite SAR system) of crossing over the Mediterranean Sea on July 4, 2001. Using the CMOD4 algorithm for the scene gives the wind velocity in 50 m resolution (Fig. 3). There is a wind velocity between 2 and 5.5 m/s. The velocity decreases
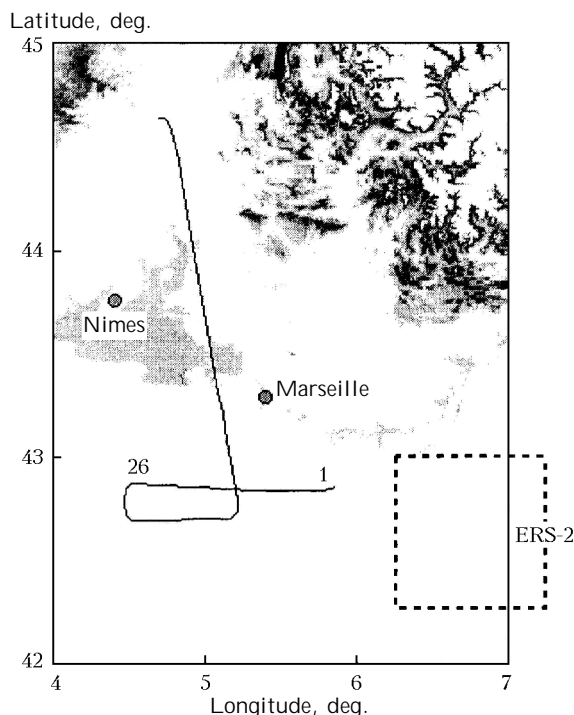

Fig. 2. Geometry of the flight path using the airborne Doppler lidar WIND and comparison with an ERS-2 SAR scene.
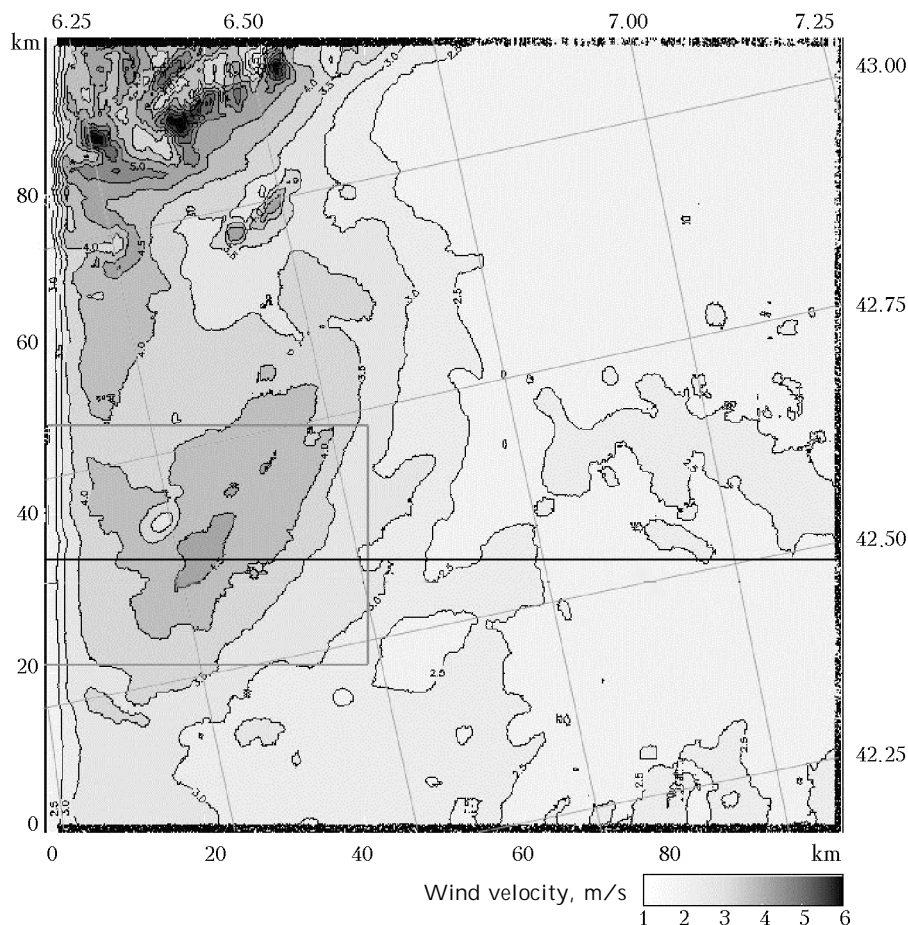

Fig. 3. Wind velocity determined for the SAR scene shown in Fig. 2.

Ch. Werner et al.

Vol. 17, No. 8 /August 2004/ Atmos. Oceanic Opt. 579

into the east direction. There are higher velocities on the coast line and around the islands. A single profile along the line at 35 km is shown in Fig. 4. One can see the decreasing of the velocity into the east direction from about 4 m/s to 2 m/s.
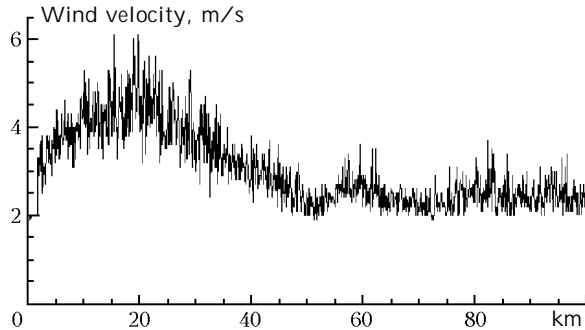

Fig. 4. Wind velocity along a line at 35 km in Fig. 3.

WIND was operated nearly in the same region (Fig. 2) but also in the same time (profile 1).

Figure 2 shows the flight path for the comparison with ERS-2 SAR swath. Starting point of the wind profile measurements is on the eastern corner of the flight track. Figure 5 shows the estimated wind profile measured at point 1 of Fig. 2. One revolution of the scanner was used to get the profile. There is normally enough aerosol over sea and especially close to the surface. The error of the single scan estimate is 1.3 m/s in wind speed and 10 degree in wind direction. Wind speed for profile 1 close to the sea surface (0−250 m) is about 5 m/s from 140 degree. For the continuation of the measurements along the flight path, Figure 6 shows the wind speed versus the scan number in the lowest level above sea of the wind profile. The scan number is also inserted in Fig. 2 on the flight track. There is a wind velocity of about 5 m/s for the profiles 1−15, and is further increasing to 10 m/s for profile 26. This is in agreement with the SAR derived wind and the tendency for higher wind speed into western direction.
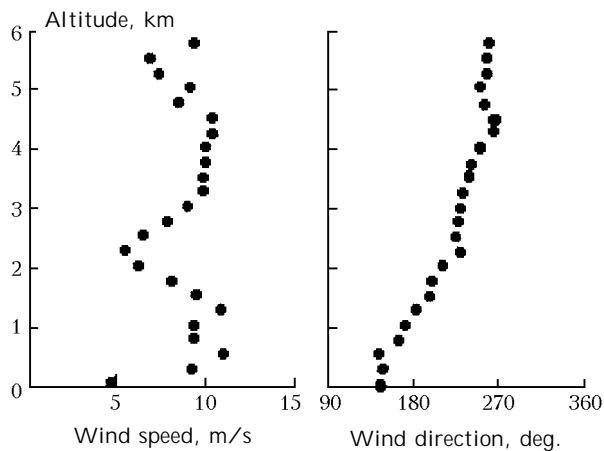

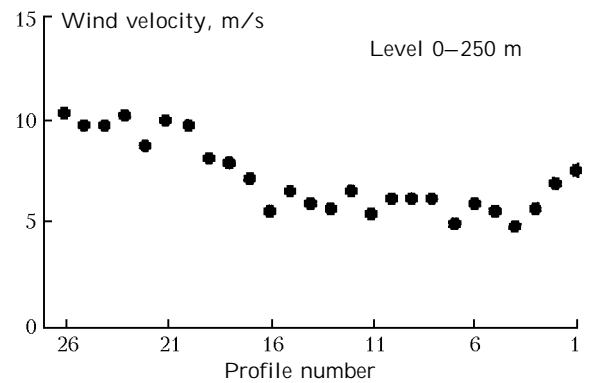**Fig. 5.** Wind profile for point 1 in Fig. 2. Wind speed (left) and wind direction (right) versus altitude.

Fig. 6. Wind speed along the flight track (see Fig. 2).

4. Restoration of turbulence parameters from SAR and lidar data

In what follows we based on the theory of atmospheric turbulence.[22–24] We propose that wind velocity fluctuations in atmosphere are isotropic and the spatial spectrum of velocity turbulent inhomogeneities is described by the von Karman's model. In accordance with this model the longitudinal $S_u(z, \kappa_z)$, transversal $S_u(z, \kappa_x)$, and two-dimensional $S_u(z, \kappa_z, \kappa_x)$ spectra can be presented as

$$S_u(z, \kappa_z) = \frac{2\sigma_u^2(z) \, L_u(z)}{[1 + (8.43 L_u(z)\kappa_z)^2]^{5/6}}, \qquad (4)$$

$$S_u(z, \kappa_x) = \frac{\sigma_u^2(z) \, L_u(z)}{[1 + (8.43 L_u(z)\kappa_x)^2]^{5/6}} \times$$

$$\times \left[1 + \frac{5}{3} \frac{[8.43 L_u(z) \, \kappa_x]^2}{1 + [8.43 L_u(z)\kappa_x]^2} \right], \qquad (5)$$

$$S_u(z, \kappa_z, \kappa_x) = \frac{1}{6\pi} \frac{\sigma_u^2(z) \, [8.43 L_u(z)]^2}{\{1 + [8.43 L_u(z)]^2(\kappa_z^2 + \kappa_x^2)\}^{4/3}} \times$$

$$\times \left[1 + \frac{8}{3} \frac{[8.43 L_u(z) \, \kappa_x]^2}{1 + [8.43 L_u(z)]^2(\kappa_z^2 + \kappa_x^2)} \right]. \qquad (6)$$

In Eqs. (4)−(6) parameters $\sigma_u^2(z)$ and $L_u(z)$ are the wind velocity fluctuation variance and the integral longitudinal scale of wind velocity correlation (the outer scale of turbulence $L_0 = 1.35 L_u$ [Refs. 8, 25]) correspondingly. In general case these parameters depend on height, that is Eqs. (4)−(6) allows one to model the statistically inhomogeneous fluctuations of wind velocity. Based on Eqs. (4)−(6) we can simulate random realizations of wind velocity by spectral method.[26,27]

The results of 2-D turbulent wind velocity field simulation in accordance with the Karman's model [Eqs. (4)−(6)] and analysis of the velocity spatial spectra are presented in Ref. 28. From these results and analysis it follows that slope of the spatial spectra of simulated wind velocity depends significantly on the spatial averaging of simulated

data and the wind shear when the mean wind velocity gradient is present. For homogeneous (constant) mean velocity the saturation of spectrum occurs in the low frequency range. But for the case of the mean wind gradient presence the spectrum increases in the low frequency range. In particularly, the low frequency wind shear spectrum increase can obey to "–5/3" power dependence similar to „–5/3" law for the inertia subrange of the Kolmogorov turbulence. Modeling of turbulent wind velocity field with the mean velocity gradient and spatial averaging of the simulated data over different scales allow to obtain different frequency dependences for the spatial spectra and compare them with the spatial spectra of wind velocity calculated based on the SAR data.

In Fig. 7 we reproduce the part of the wind velocity SAR data shown in Fig. 3 which is located above the horizontal line 20 km beginning with the left side of the pattern to the distance about 40 km.

Each value of wind velocity in Fig. 7 is obtained as result of averaging over pixel 12.5×12.5 m with the spatial resolution 50 m. It is seen from the figure that the mean velocity average over this area equals 3.84 m/s and the velocity variance is 0.95 m²/s². The wind velocity field in Fig. 7 is not homogeneous. On the average the velocity varies in the range approximately from 2 to 6 m/s, that is there is wind shear in the considered area. Using velocity values in each separate line of pixels in Fig. 7 we have calculated the 1-D random spatial spectra of wind velocity and then average them over the all lines. The result is shown in Fig. 8 as curve *4* "experiment 1". The same procedure was applied to the column of

pixels in Fig. 7. As a result we have curve *5* "experiment 2" in Fig. 8.

Assuming that wind velocity turbulent field near the sea surface obeys the Kolmogorov's law and its spatial spectrum is described by the Karman's spectral model we have simulated 1-D random realizations of wind velocity based on Eq. (4). Each realization was consisted of 524288 readings with the spatial resolution 0.1 m. The velocity variance in Eq. (4) was given $\sigma_u^2 =$ = 3.4 m²/s² and simulation was performed for the integral scale L_u = 1, 3, and 10 m. Then each realization was divided on the intervals with 500 readings in length (50 m). After that average over 125 first readings (12.5 m) was performed in each interval. The rest readings in the intervals did not take into account.

Described procedure give us, similar to SAR data, random realizations of wind velocity average over 12.5 m with spatial resolution 50 m. Obtained partially average realizations of velocity with 1048 readings in length (524288 : 500) were used for calculation of random spatial spectra. Each average simulated spectrum was obtained as a result of averaging over 50 random spectra. The results are shown in Fig. 8 by curves *1–3* for L_u = 1 m, L_u = 3 m, and L_u = 10 m.

The variance of average over 12.5 m values of wind velocity simulated for L_u = 3 m equals 1.2 m²/s² and is close to the experimental velocity variance 0.95 m²/s² in Fig. 7. Simulated spectrum for L_u = 3 m (curve *2* in Fig. 8) almost coincides with the experimental spectra in the high frequency range and strongly differs from them in the low frequency range. The discrepancy between simulated and experimental spectra in the low frequency range is caused by the effect of wind shear.
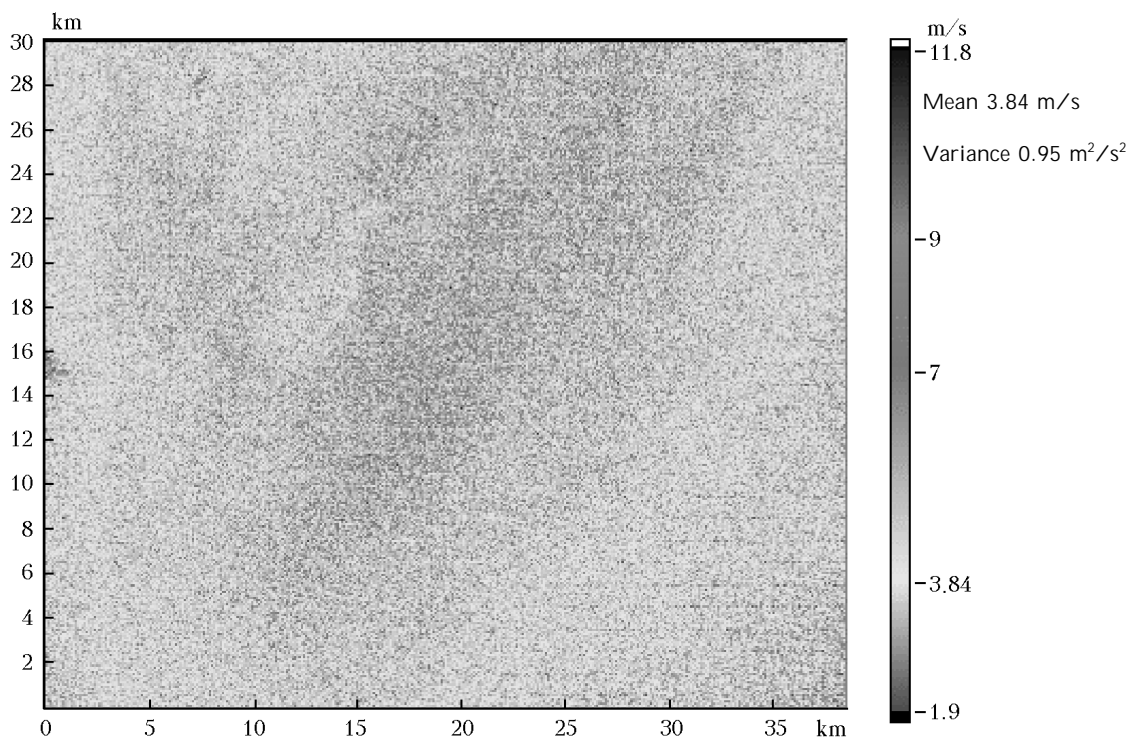

Fig. 7. 2-D wind velocity field shown in Fig. 3 as rectangular are 30×40 km above 20 km horizontal line beginning with the left side of the pattern.
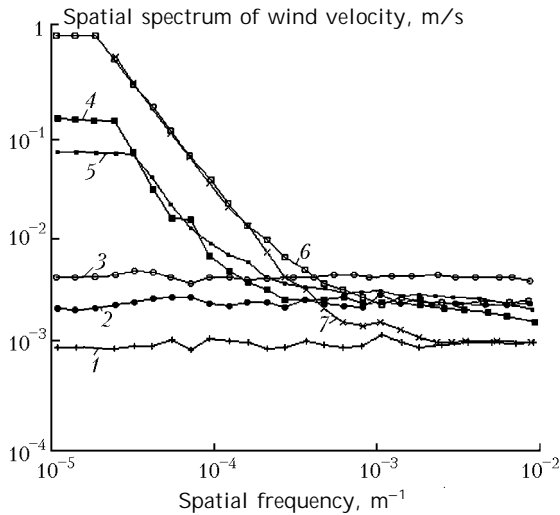
Fig. 8. Experimental and simulated spatial spectra of wind velocity calculated from SAR data: $L_u = 1$ m (*1, 7*), 3 m (*2, 6*), 10 m (*3*); experiment 1 (*4*); experiment 2 (*5*). Curves *1–3* were calculated without taking into account a gradient of the mean wind velocity, *6, 7* – with account of this gradient.

In order to take into account this effect, we have simulated random velocity with constant gradient of the mean velocity equals 5 m/s in the range from 2 to 7 m/s in accordance with the SAR data in Fig. 7. The results are shown by curves *6* and *7* for $L_u = 3$ m and $L_u = 10$ m in Fig. 8. It is seen from the figure that obtained simulated spectra have the same frequency dependence as the experimental ones in the all frequency range. Whence it follows that from fitting of the simulated spectra to the SAR experimental spectra by means of variation of the simulation parameters we can determine such turbulence parameters as outer scale of turbulence, velocity variance, and dissipation rate of turbulent energy.

In Fig. 9 we show the experimental spatial spectrum of wind velocity which is the result of average of random spatial spectra calculated from the wind velocity values in each pixel line in Fig. 7 and the modeled spectrum which is best matched to the experimental spectrum. Fitted spectrum was calculated from wind velocity data simulated for the parameters $\sigma_u^2 = 0.64$ m^2/s^2 and $L_u = 30$ m. Simulation was performed with the account for the real gradients of mean velocity along each line of SAR data in Fig. 7. From fitting of the experimental and simulated spectra in Fig. 9 we can conclude that turbulent wind velocity field near the sea surface is characterized by the parameters values, which are approximately the same as the simulation parameter values.

Turbulence energy dissipation rate ε_T is determined by the expression[23]

$$\varepsilon_T = C_L \frac{\sigma_u^3}{L_u}, \qquad (7)$$

where $C_L = 0.67$. Substituting $\sigma_u = 0.8$ m/s and $L_u = 30$ m in Eq. (7) we find that near the sea surface the dissipation rate $\varepsilon_T \approx 1.1 \cdot 10^{-2}$ m^2/s^3.
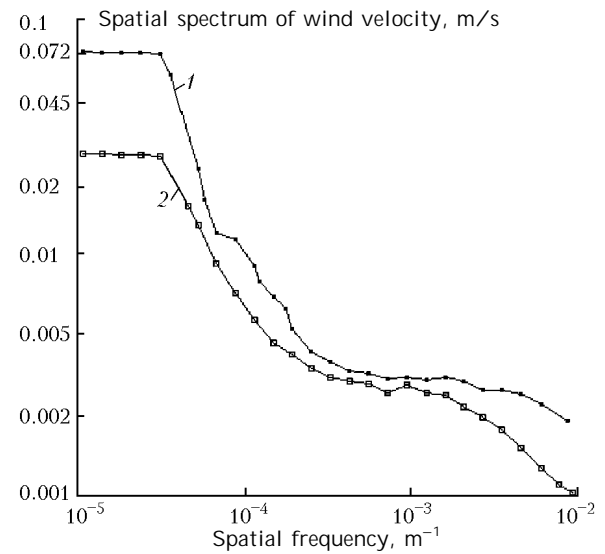

Fig. 9. Fitting of simulated spectrum to the SAR velocity spectrum: experiment (*1*); model ($\sigma_u^2 = 0.64$, $L_u = 30$ m) (*2*).

Doppler lidar estimates of LOS wind velocity component accumulated in 26 scans along flight track between points 1 and 26 in Fig. 2 with the spatial resolution 288 m (250 m in height) were used for estimation of the wind field turbulence parameters. The all array of LOS velocity estimates for the height range from 0 to 5 km was divided on four subarrays for the height ranges 0–1.25 km, 1.25–2.5 km, 2.5–3.75 km, 3.75–5 km. In each height range we estimated the structure function of wind velocity

$$D_V(r) = \langle [v(R + r) - v(R)]^2 \rangle$$

where angle brackets $\langle ... \rangle$ denote spatial averaging, by the formula

$$\hat{D}_V(r) = D_V(\Delta r N, H) =$$

$$= \frac{1}{n} \sum_{i=1}^{n} [V_{\text{LOS}}(H + \Delta r N) - V_{\text{LOS}}(H)]^2, \qquad (8)$$

In Eq. (8) $n = 200$ is the number of shots along scan circle, H is the height, $\Delta r = 250$ m, $N = 1, 2, 3, 4$. In Fig. 10 we show the calculated by Eq. (8) empirical spatial structure functions average over the all possible separations inside the each subarray of heights and over the all 26 scans.

From Fig. 10 it follows that average wind velocity structure function is saturated with increasing the observation point separation and the level of saturation increases with the height.

In any case the saturation level of the structure function in the height range 3.75–5 km exceeds the level of structure function saturation in the height range 0–1.25 km. For the Karman's model of turbulence the saturation level of wind velocity structure function is determined by the outer scale of turbulence and the variance of wind velocity fluctuations. Using the same procedure as in Ref. 29, we can fit the experimental spatial structure functions
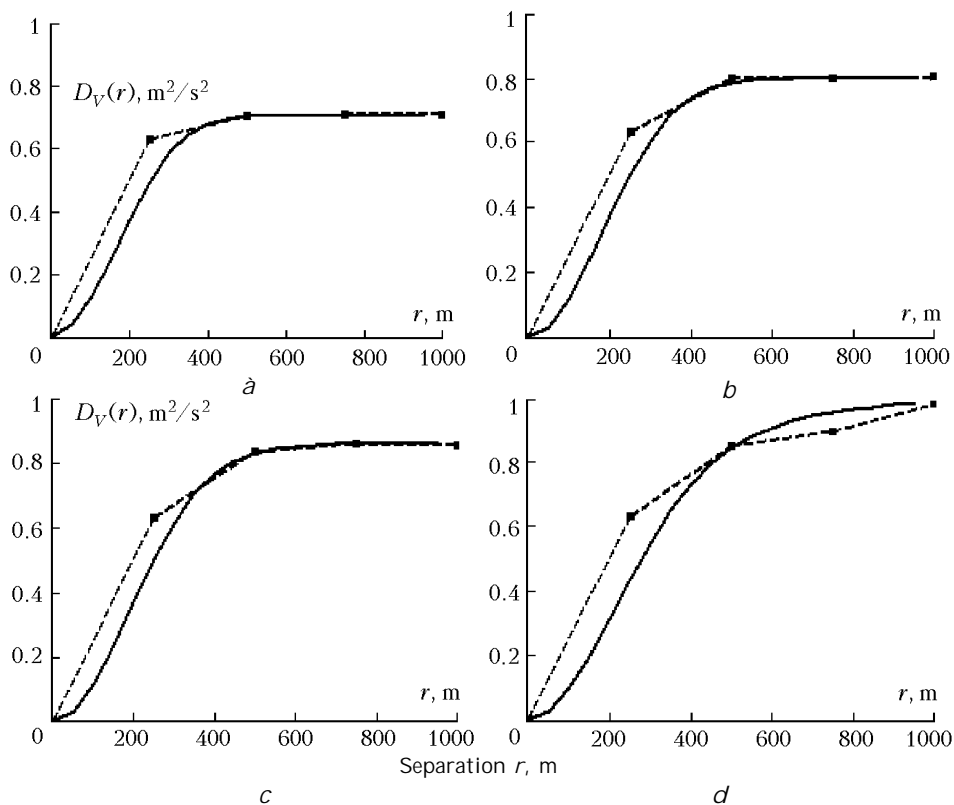
Fig. 10. Spatial structure function of LOS wind component calculated for the height ranges: 0–1.25 (*à*), 1.25–2.5 (*b*), 2.5–3.75 (*c*), and 3.75–5.0 km (*d*). – – – – – – is experiment; ——— is simulation for L_u = 130 m, σ_u = 1.9 m/s (*à*); 220 m, 1.3 m/s (*b*); 310 m, 1.2 m/s (*c*); 330 m, 1.0 m/s (*d*).

to the modeled ones and determine the turbulent parameters L_u and σ_u^2 for which the fitting is best. The found values of L_u and σ_u^2 we can take as estimates of these parameters.

The results of fitting are shown in Fig. 10 by solid curves. The estimates of the turbulent energy dissipation rate are derived based on Eq. (7) as a result of substituting the found values of L_u and σ_u^2 in that equation. Table contains the estimates of the dissipation rate. For lower layer 0–1.25 km ε_T is maximal and takes the value $\varepsilon_T = 3.5 \cdot 10^{-2}$ m^2/s^3 approximately. It is rather close to the estimation of ε_T obtained from SAR velocity data ($\varepsilon_T = 1.1 \cdot 10^{-2}$ m^2/s^3 approximately). Estimates of ε_T decrease with the height and its values do not contradict to the atmospheric turbulence theory and known measurement results.

Range, km	Integral scale $L_{u,}$ m	Wind velocity standard deviation $\sigma_{u,}$ m/s	Dissipation rate $\varepsilon_{T,}$ m^2/s^3
0–1.25	130	1.9	$3.5 \cdot 10^{-2}$
1.25–2.5	220	1.3	$6.7 \cdot 10^{-3}$
2.5–3.75	310	1.2	$3.7 \cdot 10^{-3}$
3.75–5.0	330	1.0	$2.0 \cdot 10^{-3}$

Summary

There is a reasonable agreement between SAR derived wind over sea surface (between 2.5 m/s and 5 m/s) and the airborne Doppler lidar wind (between 5 m/s and 10 m/s) close to the surface. The trend for higher wind speed in the western direction can be seen in larger altitudes too. With a calibrated airborne Doppler lidar one can measure wind profiles over sea with the connection to the surface layer given for example by SAR devices with a better horizontal resolution and a larger coverage. This is a first result from one single example. Statistics for a better understanding of both wind sensors and their combination for data assimilation for weather forecast will be available in the near future (Thorpex experiment 2003). Evaluation of the turbulent parameters based on estimation of the spatial structure function of measured LOS component of wind velocity shows that the WIND system allows to get information not only on the mean wind but to estimate the wind turbulence parameters as well.

It is shown that the spatial spectra of wind velocity near the sea estimated from ERS-2 SAR measurement data increase in the range of low spatial frequencies. From comparison of the obtained experimental SAR velocity spectra with the results of computer simulation of random wind velocity fields it follows that this low frequency increase of the experimental spectra is caused by the wind shear. By means of fitting of the simulated spatial spectra of wind velocity to the SAR velocity spectra the estimates of the wind velocity variance, the integral longitudinal scale, and the turbulent energy dissipation rate near the sea surface are found in the paper. It

Ch. Werner et al.

Vol. 17, No. 8 /August 2004/ Atmos. Oceanic Opt. 583

occurs that the dissipation rate values estimated from the SAR and lidar data measured simultaneously over approximately the same area of the Mediterranean Sea are close to each other.

Acknowledgments

References

1. A. Stoffelen and D. Anderson, in: *Proc. 2nd ERS-1 Symposium: Space at the Service of our Environment* (Hamburg, 1993), pp. 997−1001.
2. M. Hardesty and J.M. Intrieri, in: *Proc. COMEAS 95* (Atlanta, Ga, Piscataway, NJ:IEEE, 1995), pp. 148−150.
3. S.Lehner, J. Horstmann, W. Koch, and W. Rosenthal, J. Geophys. Res. **104**, 7847−7856 (1998).
4. Ch. Werner, S. Rahm, S. Lehner, M. Buchhold, V. Banakh, and I. Smalikho, Pure and Appl. Opt. **7**, 1473−1487 (1998).
5. Ch. Werner, P. Flamant, O. Reitebuch, C. Loth, F. Köpp, P. Delville, Ph. Drobinski, J. Streicher, B. Romand, H. Herrmann, E. Nagel, Ch. Boitel, M. Klier, D. Bruneau, M. Messionnier, S. Rahm, A. Dabas, D. Oh, and M. Lopez, Opt. Eng. **40**, 115−125 (2001).
6. O. Reitebuch, Ch. Werner, I. Leike, P. Delville, P.H. Flamant, A. Cress, and D. Engelbart, J. Atmos. Ocean. Technol. **18**, 1331−1344 (2001).
7. R.G. Frehlich, S. Hannon, and S. Henderson, Boundary-Layer Meteorol. **86**, 233−256 (1998).
8. R. Frehlich and L. Cornman, J. Atmos. Oceanic Technol. **19**, 355−366 (2002).
9. V.A. Banakh, I.N. Smalikho, F. Köpp, and Ch. Werner, J. Atmos. Oceanic Technol. **16**, 1044−1061 (1999).
10. F. Drobinski, A.M. Dabas, and P.H. Flamant, J. Appl. Meteorol. **39**, 2434−2451 (2000).
11. R.L. Schwiesow, F. Köpp, and Ch. Werner, J. Atmos. Ocean. Technol. **2**, 3−14 (1985).
12. J.W. Bilbro, C. DiMarzio, D. Fitzjarrald, S. Johnson, and W. Jones, Appl. Opt. **25**, 3952−3987 (1986).
13. J. Bilbro, G. Fichtl, D. Fitzjarrald, and M. Krause, Bull. Amer. Meteorol. Soc. **65**, 348−359 (1984).
14. J.W. Bilbro and W.W. Vaughan, Bull. Amer. Meteorol. Soc. **59**, 1095 (1978).
15. E.W. McCaul and R.J. Doviak, *Accuracy of aircraft position and motion data from inertial navigation equipment aboard the NASA CV 990.* NASA Final Report, Contract No. H-84050B (1988).
16. D.M. Tratt, R.T. Menzies, M.P. Chiao, D.R. Cutten, J. Rothermel, R.M. Hardesty, J.N. Howell, and S.L. Durden, Appl. Opt. **41**, 6941−6949 (2002).
17. J. Rothermel, D.R. Cutten, R.M. Hardesty, R.T. Menzies, J.N. Howell, S.C. Johnson, D.M. Tratt, L.D. Olivier, and R.M. Bant, Bull. Amer. Meteorol. Soc. **79**, 581−599 (1998).
18. R.B. Targ, C. Steakley, J.G. Hawley, L.L. Ames, P. Forney, D. Swanson, R. Stone, R.G. Otto, V. Zarafis, P. Brockman, R.C. Calloway, S.H. Klein, and P.A. Robinson, Appl. Opt. **35**, 7117−7127 (1996).
19. S. Rahm, Opt. Lett. **20**, 216−218 (1995).
20. A. Dabas, P. Drobinski, O. Reitebuch, E. Richard, P. Delville, P.H. Flamant, and Ch. Werner, Geophys. Res. Lett. **30**, 21-1−21-4 (2003).
21. J.M. Wright, IEEE Trans. Antennas Propag. AP-14, 749−754 (1996).
22. J.O. Hinze, Turbulence: *An Introduction to Its Mechanism and Theory* (McGraw-Hill, 1959), 586 pp.
23. A.S. Monin and A.M. Yaglom, *Statistical Fluid Mechanics. Part 2. Mechanics of Turbulence* (Moscow, Nauka, 1965), 720 pp.
24. N.K. Vinnichenko, N.Z. Pinus, S.M. Shmeter, and G.N. Shur, *Turbulence in the Free Atmosphere* (Consultants Bureau, 1973), 263 pp.
25. D.H. Lenschow and L. Kristensen, J. Atmos. Oceanic Technol. **5**, 715−726 (1988).
26. V.A. Banakh and I.N. Smalikho, Atmos. Oceanic Opt. **10**, No. 12, 957−965 (1997).
27. R. Frehlich, J. Atmos. Oceanic Technol. **14**, 54−75 (1997).
28. V.A. Banakh and A.V. Falits, Atmos. Oceanic Opt. **16**, No. 8, 649−651 (2003).
29. V.A. Banakh and A.V. Falits, Atmos. Oceanic Opt. **17**, No. 4, 260−267 (2004).